Towards *in-situ* U–Pb dating of dolomites

Bar Elisha[1,3], Perach Nuriel[1], Andrew Kylander-Clark[2], Ram Weinberger[1]

[1]Geological Survey of Israel, Jerusalem, Israel
[2]Department of Earth Sciences, University of California, Santa Barbara, CA, USA
[3]Department of Natural Sciences, The Open University of Israel

Correspondence to: Bar Elisha (brelisha@gmail.com)

Abstract. Recent U–Pb dating by laser ablation ICP-MS has demonstrated that reasonable precision (3–10% 2σ) can be achieved for high-resolution dating of texturally distinct calcite phases. Absolute dating of dolomite, for which biostratigraphy and traditional dating techniques are very limited, remains challenging but may resolve many fundamental questions related to the timing of mineral-rock formation by syngenetic, diagenesis, hydrothermal, and epigenetic processes. In this study we explore the possibility of dating dolomitic rocks via recent LA-ICP-MS dating techniques developed for calcite. The *in-situ* U–Pb dating was tested on a wide range of dolomite rocks of various origins (i.e., syngenetic, early diagenetic and epigenetic) from the Cambrian to Pliocene age—all of which from well-constrained stratigraphic sections in Israel. We present *in-situ* U–Pb results of dolomitic rock samples, together with imaging techniques and chemical characterizations. We show that dolomite dating is highly sensitive to textural differences and highlight parameters such as crater morphology and roughness, calcite zoning and impurities that may affect the interpretation of the resulted ages. Textural examination indicates zonation and mixing of different phases at the sub-millimeter scale (<1 µm), and thus Tera-Wasserburg ages may represent mixing dates of early diagenesis and some later epigenetic dolomitization event(s). We conclude that age mixing at the sub-millimeter scale is a major problem in dolomite dating that need to be further studied and note the necessity of matrix-matched standards for accurate dating.

1 Introduction

Dolomite is vastly abundant in exposed stratigraphic sequences, and its manifestation in the geological record increases towards older sedimentary strata (Warren, 2000). Nonetheless, it is very rare in modern environments and has never been successfully grown in laboratory experiments at near-surface conditions (Machel, 2004, and references therein). Although the conditions and kinetics promoting dolomite growth are not well understood, its formation is considered as a by-product of a chemical reaction between Mg-rich fluids and calcite-bearing rocks. Previous studies suggested that dolomite is being formed either by diagenetic replacement of limestone during deposition (syngenetic; Sass, 1969), soon after deposition (early diagenetic; Ahm et al., 2018; Frisia et al., 2018), or at later stage (epigenetic; Sibley and Gregg, 1984). Distinguishing between different dolomitization processes is challenging, yet critical for resolving some of the issues and ambiguities related to the formation of dolomitic rocks. Accurate U–Pb absolute dating of dolomite by laser ablation inductively coupled plasma mass

spectrometry (LA-ICP-MS) could contribute to better understanding of dolomitization process by placing these event(s) in the proper geological context.

Recent developments of LA-ICP-MS has opened a new avenue for measuring absolute ages of carbonates but are mostly applied to calcite. By determining absolute ages, U–Pb calcite geochronology has improved the understanding of many
35   fundamental geological processes, such as fossilization (Li et al., 2014), tectonic faulting (Ring et al., 2016; Roberts and Walker., 2016; Nuriel et al., 2017; Parrish et al., 2018), duration of sedimentation, and diagenesis (Hodson et al., 2016; Godeau et al., 2018). Despite the low concentrations of U and radiogenic Pb in carbonates (<10 ppm and <2 ppm, respectively) and the considerable amounts of common Pb (up to 100 ppm), a reliable age determination of calcite is obtained via isochrone regression on a Tera-Wasserburg inverse concordia diagram (Tera and Wasserburg, 1972). By this method, the common-Pb
40   composition and the age are simply determined by the upper and lower intercept of the regression isochrone with the concordia curve, respectively. While LA-ICP-MS calcite evolved to be a conventional method (Roberts et al., this issue), a thorough methodology for dating other carbonates, such as dolomite, is still in progress (Guillong et al., this issue).

Dating dolomitic rocks is more challenging than calcite, particularly because their complicated growth history is often characterized by the formation of multi-phase microcrystalline grains (e.g. partial replacement, zoning). Growth-zones cannot
45   be separated physically, and their size is often smaller than the diameter of the laser spot (usually >50 μm). In addition, well-characterized dolomite reference materials (RM) are currently unavailable for the LA community and differences between calcite and dolomite in terms of matrix-effect and plasma efficiency are not well understood (Guillong et al., this issue). In order to examine the effect of using common RM and the suitability of conventional LA-ICP-MS calcite procedure for dolomite geochronology, we use dolomitic rock samples with well-defined stratigraphic ages. We show differences in texture,
50   crater morphology, impurities, and down-hole fractionation trends, between RMs and dolomite and discuss textural characteristics and chemical properties of successful and unsuccessful dolomite dating. Finally, we consider the age results in the geological context of the studied rocks.

1.1 Studied dolomites

Dolomitic rocks in Israel and environs include syngenetic to early diagenetic dolomites, epigenetic dolomites, hydrothermal
55   dolomites and mixed/hybrid ones, whereas their ages are well constrained by field relations and dates of adjacent geological unites (Fig. 1).
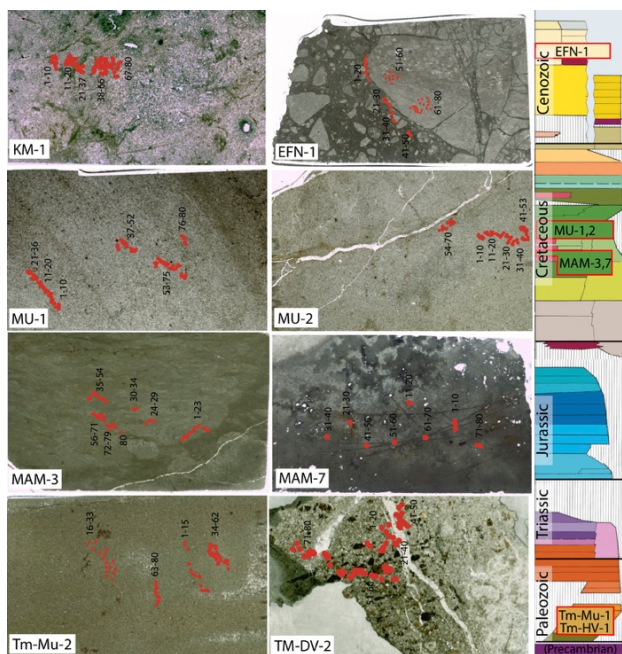
Figure 1: Photomicrographic of thin sections of studied samples, showing the locations of LA-ICP-MS analyses (red dots). Width of thin-sections are 27 mm. Sample locations along the stratigraphic column of Israel is presented in the right panel.

60 ### 1.1.1 Syngenetic Cambrian dolomites and hydrothermal dolomites (Timna Valley)

Precambrian crystalline basement rocks of the Arabian-Nubian Shield are exposed in southern Israel and are unconformably overlain by Cambrian sediments (Fig. 1; Beyth et al., 1999). In the Timna Valley, southern Israel, Cambrian dolomitic rocks of the Timna Formation are well-known for their copper deposits and ancient to present-day mining and are considered to be epigenetic in nature (Segev, 2016). Dolomitic rocks of the Timna Formation (sample Tm-MU-2; Fig. 1) represent the earliest

65 oceanic transgression in the area, constrained by trilobite borrowing to upper Georgian (~520 Ma; Parnes, 1971) and by a subvolcanic intrusion dated to ~532 Ma (Beyth and Heimann, 1999). Sample Tm-MuU-2 (Fig. 1) is composed of reddish micritic dolomite of <10 μm in size, with minor iron-oxides scattered within the sample. Dolomite veins of later epigenetic diagenesis (Sample Tm-DV-1) are found in the crystalline basement rock and sandstones in Timna Valley, in association with copper, quartz, calcite and Mn and Cu-carbonates. Sample Tm-DV-1 is composed of euhedral zoned dolomite crystals of up

70 to 200 μm, with opaque cores and transparent rims. These euhedral dolomite crystals of epigenetic open-space filling cements, associated with Cu mineralization, are inferred here as the result of low-temperature (~260 °C; Beyth et al., 1997) hydrothermal activity and mineralization that assumed to occur during Neogen Times (Kohn et al., 2019).

1.1.2 Syngenetic and early diagenetic dolomites (Mount Carmel and Umm el Fahm Ridge)

Dolomitic rocks dominate the exposed Cretaceous sequence of Mount Carmel, Umm el Fahm Ridge and Judean Hills, which

75 were part of an extensive shallow carbonate platform.

The studied Cenomanian dolomitic rocks of the Deir Hanna Formation (Fig. 1) are exposed on the SE flank of the Umm el Fahm anticline near the village of Mei-Ami (Sass et al., 2013). These rocks are underlain and overlain by volcanic flows that are dated to 99 ± 0.5 and 95 ± 0.5 Ma, respectively (Ar–Ar; Segev et al., 2002). They were described as syngenetic dolomites based on preferred orientations of dolomite grains, with a c-axis maximum perpendicular to the bedding planes (Sass, 1969).

80 Samples MAM-3 and MAM-7 (Fig. 1) are composed of fine-grained (<10 μm) micritic dolomite, which reflect continuity of reefs along fine-grained, well-bedded shelf basin rocks (Sass and Bein, 1978).

Dolomitic rocks of the Zikhron Formation from Mount Carmel are considered 'early diagenetic' (Sass and Bein, 1978; Segev and Sass, 2009; Fig. 1) and crop out between two volcanic flows of 97 ± 0.5 and 95 ± 0.5 Ma (Segev, 2009). Samples MU-1 and MU-2 (Fig. 1) are composed of ~40 μm dolomite grains and represent sparry dolomite mosaic of similar ages as MAM-3

85 and MAM-7. Dolomitic rocks from the Albian Yagur Formation crop out near the Kerem Maharal village and are overlain by the oldest (99 Ma) volcanic flow known in Mount Carmel. Samples KM-1 (Fig. 1) is another sparry dolomite with ~60 μm dolomite grains and is also considered as 'early diagenetic' dolomite.

1.1.3 Epigenetic dolomites – (Judean Desert)

Strata of dolomitic rocks are abundant at the western margin of the Dead Sea basin and include the Cenomanian Hevion, Zafit

90 and Tamar formations (Sneh and Avni, 2016). These dolomitic rocks are considered 'epigenetic' dolomites that were later faulted during the activity along the Dead Sea fault. Dolomite-cemented breccias were sampled along one of the major faults of the Dead Sea western margin fault zone (En Feshkha Fault; sample EFN-1; Fig. 1) and preserve microstructures of dolomite fragments of mosaic (sparry) dolomite bounded by sparry dolomite matrix.

2 Methods

95 For LA-ICP-MS analyses of dolomites we prepared 40 μm thick thin sections polished to 1 μm. U–Pb LA-ICP-MS analyses were performed at the Department of Earth Science, University of California, Santa Barbara, following the analytical procedure described in Nuriel et al., (2017) for calcite-bearing rocks. Samples were ablated using a *Photon Machines* 193 nm ArF Excimer laser equipped with a HelEx ablation cell and coupled to a *Nu Instruments Plasma 3D* multi-collector ICP-MS. Both RMs and unknowns were ablated with similar crater size of 85 μm and fluence of ~1 J/cm^2. In order to remove any

100 contaminants, and especially common Pb from the sample surface all samples were cleaned with methanol and pre-ablated (4 times) prior to a 20 s baseline. Material was then ablated for 15 seconds at 10 Hz, resulting in a pit depth of ~15 μm. On the MC-ICP-MS, masses ^{202}Hg, ^{204}Pb, ^{206}Pb, ^{207}Pb, and ^{208}Pb were measured on Daly detectors, and masses ^{232}Th and ^{238}U were measured on Faraday detectors at low resolution (300, 10% valley definition) using an integration time of 100 ms. We used a two-steps standardization technique using NIST614 glass and the WC-1 calcite reference material (Roberts et al., 2017)

105 following the procedure outlined in Nuriel et al. (2017). Data were reduced using Iolite v. 2.5 (Paton et al., 2010) and the ^{238}U/^{206}Pb and ^{207}Pb/^{206}Pb isotopic ratios for each analysis were plotted on Tera–Wasserburg diagrams using Isoplot and

IsoplotR (Ludwig, 2012; Vermeesch, 2018); U and Pb concentrations were calculated semi-quantitively, using NIST614 as the primary RM. Secondary calcite RMs—ASH-15 (2.9646 ± 0.011 Ma; Nuriel et al., this issue) and Duff Brown (64 ± 0.67 Ma; Hill et al., 2016)—yielded dates within uncertainty of their accepted values (ASH-15: 2.973 ± 0.090, MSWD = 1.3, n = 107; Duff Brown: 63.2 ± 2.3 Ma, MSWD = 1.9, n = 106). The Pb concentration for each spot analysis was calculated by the total counts of Pb isotopes, compared to the NIST glass value (2.32 ppm). The ^{204}Pb concentration was calculated using the ^{206}Pb concentration and assuming a Stacy-Kramers ^{206}Pb/^{204}Pb ratio to avoid any issues with Hg contamination.

Following LA analyses, we used several techniques to characterize the studied dolomite samples in detail. Whole-rock analyses of Rare Earth Element (REE) composition was done on Perkin Elmer NexION 300D ICP-MS instrument. Dolomite powders were dissolved, evaporated, and diluted ~3000 in 0.1N nitric acid solution before mixed with Rh/Rn internal standards. The raw data were corrected for blank, drift and isobaric interferences and converted into concentrations in ppm using USGS reference material. The overall uncertainties are estimated to be less than 5%.

Imaging of the LA craters and identifying major phases in the samples was performed by using a field-emission FEI Scanning Electron Microscope (SEM) at the Ilse Katz Institute for Nanoscale Science & Technology at Ben-Gurion University of the Negev, Israel, with 3 kV acceleration voltage and 0.1 nA current. This device is equipped with EDS detector and 'Oxford' EBSD sensor, used for producing crystallographic phase maps. For EBSD mapping, the instrument was setup to 15 kV accelerating voltage and 26 nA current, 70˚ tilt, 2x2 binning and 0.1 μm step size. Wave Dispersion Spectroscopy (WDS) maps were preformed using a JEOL microprobe at the Hebrew University, Israel, with accelerating voltage of 15–25 kV, beam current of 80 nA, step size of 0.5 μm and dwell time of 0.35 s.

X-ray diffraction (XRD) patterns were acquired in Bragg-Brentano geometry at the Geological Survey of Israel using a PANalytical X'Pert diffractometer with CuKα radiation operated at 45 kV and 40 mA. Samples were scanned from 3 to 70° 2θ at a step size of 0.013° 2θ, using a PIXcel detector in continuous scanning line (1D) mode with an active length of 3.35°. The equivalent time per step was ~30 sec, resulting in a total measurement time of about 10 min per scan. Mineral phase identification and semi-quantification was performed using HighScore Plus® software based on ICSD database.

3 Results and Discussion

3.1 U–Pb ages and chemistry of dolomites

We present U–Pb ages of eight dolomite samples on a 'Tera-Wasserburg' inverse concordia diagrams as ^{207}Pb/^{206}Pb and ^{238}U/^{206}Pb linear regression isochrons (Fig. 2). The ^{207}Pb/^{206}Pb (Common Pb) values where not anchored to specific values and range between 0.7862 ± 0.0033 and 0.9683 ± 0.0071. MSWD values are between 0.27 and 41. For each sample, the whole-rock and single spot U and Pb content are plotted (Fig. 3A). We then classify the samples based on whole-rock chondrite-normalized REE pattern (Fig. 3B) and discuss the results in terms of likelihood for successful dating.
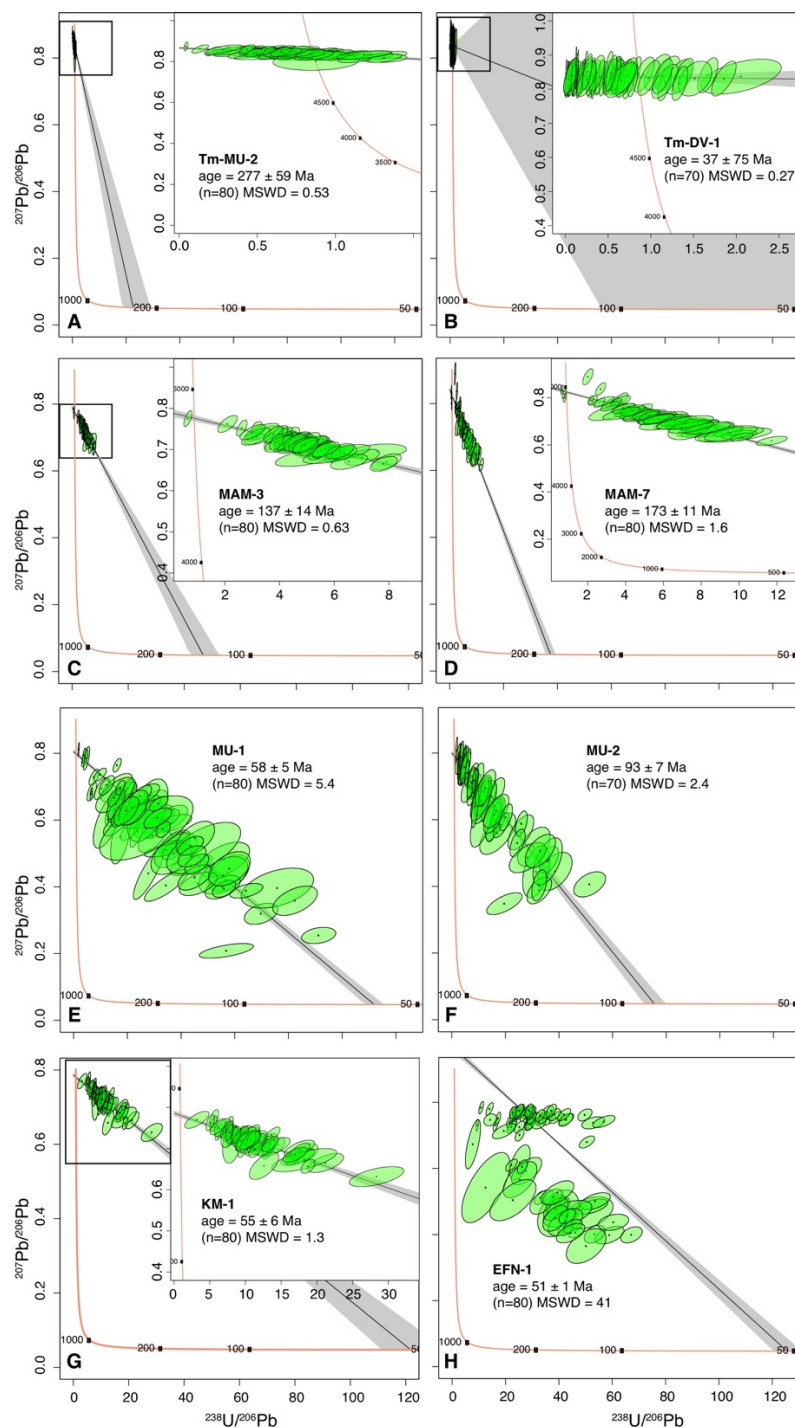
Figure 2: Tera-Wasserburg concordia plots of studied dolomites: syngenetic Cambrian dolomites (A), hydrothermal dolomites (B), syngenetic Cretaceous dolomites (C–D), early diagenetic dolomites (E–G) and epigenetic dolomite (H). All diagrams have similar axes. Isochrons and errors are presented as black lines and gray areas, respectively. Insets show enlargements of ellipse concentration areas. Error ellipsoids of spot analysis are plotted in green and represent 2σ uncertainties.

Sample	Petrographic description	Stratigraphic age	U–Pb age	MSWD	Common Pb value
Tm-MU-2	Micritic	Cambrian	277 ± 59	0.53	0.8664 ± 0.0061
Tm-DV-1	Hydrothermal	Miocene	37 ± 75	0.27	0.8385 ± 0.0038
MAM-3	Micritic	Cretaceous	137 ± 14	0.63	0.7899 ± 0.0047
MAM-7	Micritic	Cretaceous	173 ± 11	1.6	0.8427 ± 0.0032
MU-1	Sparry	Cretaceous	58 ± 5	5.4	0.8046 ± 0.0036
MU-2	Sparry	Cretaceous	93 ± 7	2.4	0.8064 ± 0.004
KM-1	Sparry	Cretaceous	55 ± 6	1.3	0.7862 ± 0.33
EFN-1 fragments	Sparry	Pleistocene	74 ± 3	0.99	0.8140 ± 0.021
EFN-1 Matrix	Sparry	Pleistocene	6.5 ± 1	1.5	0.7853 ± 0.0047

Table 1: Sample description and stratigraphic age and their corresponding LA results.

The U–Pb isotopic ratios of spot analyses of the epigenetic Cambrian dolomite Tm-MU-2 forms isochron that intercept at 277

145   ± 59 (MSWD = 0.53; n = 80; Fig. 2A), with a common Pb value of 0.8664 ± 0.0061. This sample was expected to generate Cambrian dolomite age, but even if considering its large error (± 59 Ma), the result is ~180 Ma younger. The large error on the isochron is due to high count rates of common Pb, whereby error ellipses are plotted near the common Pb value with no radiogenic Pb. Consequently, the lower intercept is far projected and poorly constrained. Data point analytical uncertainties are, however, smaller than the scatter of the spot analysis and the MSWD of 0.53 represent a fairly reasonable isochrone. The

150   low common Pb value may represent incorporation of radiogenic Pb derived from the surrounding crystalline rocks, as expected for hydrothermal carbonates (Stacey and Kramers 1975). The REE signature of sample Tm-MU-2 show enrichment in LREE, depletion in HREE and positive Gd anomaly (Figure 3B). This pattern is similar to other dolomite samples in this study, although one order of magnitude higher, suggesting that dolomitic rocks in association with hydrothermal activity have high common Pb content, and thus, low-chance for successful dating.

155   The U–Pb data of the hydrothermal dolomite sample Tm-DV-1 shows similar pattern with Tm-MU-2, with lower intercept age of 37 ± 75 (MSWD = 0.27; n = 70; Fig. 2B) and common Pb value of 0.8385 ± 0.0038. Spot analysis within this sample are plotted in the upper-left quadrant in figure 3A, with low U (~0.2 ppm) and high Pb contents (~5 ppm). We define samples that plot within these U and Pb values as low-chance for successful dating.

Syngenetic Cretaceous dolomite samples MAM-3 and MAM-7 yielded a 'small scale isochron' (Ring and Gerdes, 2016), with

160   lower intercept age of 137 ± 14 (MSWD = 0.63; n = 80) and 170 ± 11 (MSWD = 1.6; n = 80) and common Pb value of 0.7899 ± 0.0047 and 0.8427 ± 0.0032, respectively (Figure 2C–D). The stratigraphic age for these samples is constrained to 99 and 95.4 Ma (Segev et al., 2002), however, U–Pb ages are 40% to 70% older than expected. In these samples, U and Pb contents plot close to 1 ppm U, but their total Pb content is up to 20 ppm (Figure 3A). Although the low $^{207}Pb/^{206}Pb$ value of 0.7899 in sample MAM-3 indicate higher incorporation of radiogenic-Pb during dolomitization compared to sample MAM-7 (0.8427 ±

165   0.0032), MAM-7 displays a much larger age offset than MAM-3. Following the results of Guillong et al. (this issue), the

observed age offsets can be explained by different ablation efficiency for these samples, compared to the standards. As these samples are micritic dolomites, with crystal size of <10 μm, they tend to ablate much efficiently compared to WC-1. Guillong et al. (this issue) noticed that 160% ablation efficiency in micritic dolomite compared to WC-1 results in age offset of 4–8%. Our samples display a much higher offset range of 40–70% and will be further discussed in section 3.5.

170   In opposed to the previous micritic-textured Cretaceous samples, the U–Pb ages of the sparry sample MU-2 yielded a lower intercept age of 93 ± 7 and common Pb value of 0.8064 ± 0.004 (MSWD = 2.4; n = 70; Fig. 2F). This age is slightly younger than the 95–97 Ma Ar-Ar ages of the constraining volcanic layers, but fairly within error limits. Sample MU-1 from a nearby location yielded much younger intercepts age of 58 ± 5 Ma with large uncertainty and common Pb value of 0.8046 ± 0.0036 (MSWD = 5.4; n = 80; Fig. 2E). As the ablation efficiency of sparry dolomites does not considerably vary from WC-1, the

175   consistent age of MU-2 and the younger age of MU-1 appear to represent actual diagenesis/dolomitization processes and the resulted ages of these samples are further discussed in section 3.5. The U content of these samples is between 0.5 to 2 ppm and Pb content is between <0.1 and 4 ppm, forming a cluster around the center of the diagram in Figure 3A. The sparry sample KM-1, constrained stratigraphically to 99 Ma, shows similar age pattern to sample MU-1, with lower intercept age of 55 ± 6 (MSWD = 1.3; n = 80; Fig. 2G) and common Pb value of 0.7862 ± 0.033. The REE signature of the above three samples are

180   rather similar, with slightly elevated LREE and similar Gd anomaly (Figure 3B).

Analyses on the fault related epigenetic dolomite (sample EFN-1 Judean Desert) was performed along two targets: the homogeneous sparry dolomitic fragments (n = 30) and the fine grained enclosing dolomitic matrix between fragments (n = 50). Because spot analyses are clearly a mix from two different phases the U–Pb age result for of all 80 spot analyses represent a mixed age of 51 ± 1 Ma (MSWD = 41; n = 80) and upper intercept value of 0.9683 ± 0.0071 (Figure 2H). Ellipses in these

185   sample arrayed along two isochrones and the meaning of these results are also further discussed below.
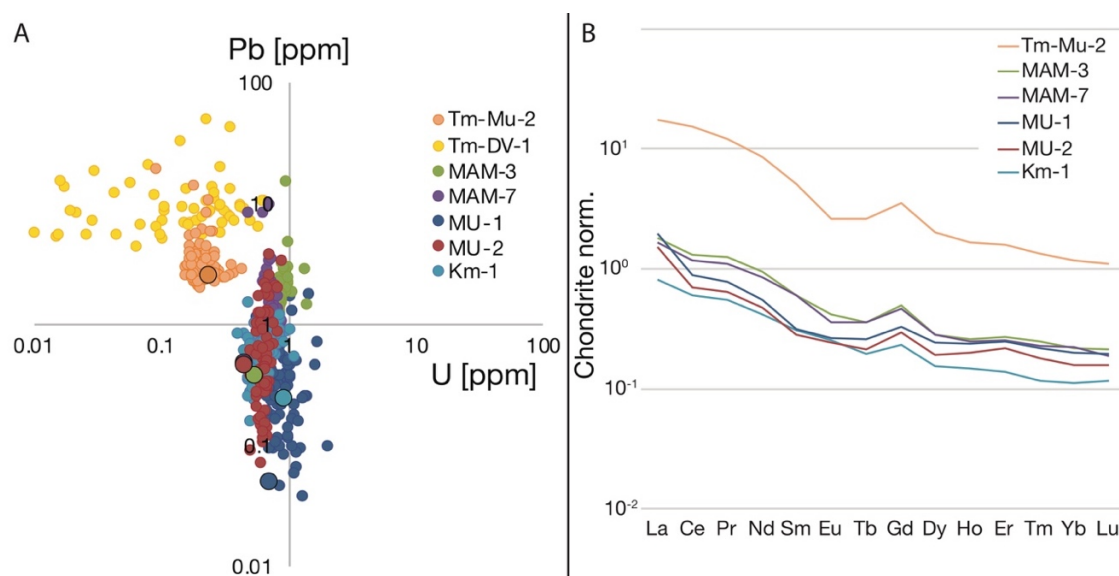
Figure 3: (A) U vs. Pb [ppm] of single spots analyses by LA-ICP-MS of studied dolomite samples, together with whole rock U and Pb content of each sample (large circles). (B) Corresponding whole-rock REE patterns normalized to chondrite values.

3.2 Textural characteristics effecting ablation efficiency

190 Dolomite and calcite resemble in many of their crystallographic and chemical properties, however, these minerals interact differently with the laser beam. Successful LA analysis is dependent on ablation efficiency, as differences in crater morphology between unknowns and RM may cause mass fractionation due to uneven mass removal and imperfections in crater rims and bottom. Accordingly, differences in particle size and volume of mass introduced to the ICP-MS torch can significantly affect the resulted age. Guillong et al. (this issue) suggest that differences in crystal size may result in ablation rate of up to 160%

195 higher relative to WC-1, with age offsets of 4–8 % for dolomite. Variations in crater size between RM and unknowns for identical laser parameters dolomite might shift $^{238}U/^{206}Pb$ ratios to lower values and older ages (Guillong et al., this issue). Spots of the studied dolomites were imaged here by 50˚ tilted SEM stage and the shape of crater rims and bottom is corelated with the age results (Fig. 4). Most craters display relatively similar patterns, but in samples with poorly constrained ages numerous craters were identified with rough bottom and imperfections of the rims. Crater bottom roughness was classified as

200 smooth, moderate or rough, in comparison to WC-1. We find that dolomitic rocks with crystals larger than 10 μm behave similarly to calcite, resulting in comparable aspect ratios of craters (crater depths/crater diameter) to that of WC-1, but rougher crater bottom and rim (Fig. 4A–B). U–Pb analyses of sparry sample MU-2 resulted in an age of 93 ± 7 Ma, that is very similar to the stratigraphic age of 97–95 Ma. The shape of the crater in this sample was similar to crater shape in the standard and yielded a reasonable age. On the other hand, micritic dolomites with <10 μm grain-size ablate much faster than sparry dolomite

205 and WC-1, resulting in deeper and rougher laser craters. Rough crater bottom with high aspect ratio appear to result in standard underestimation and age overestimation, as can be seen in the micritic samples MAM-3 and MAM-7. These samples were expected to produce Cretaceous ages between 100 to 90 Ma but resulted in much older ages of 137 ± 14 and 173 ± 11 Ma. All the above variables translate into underestimation or overestimation of the standard correction and must be considered when defining a matrix-matched standard for dolomite.

210
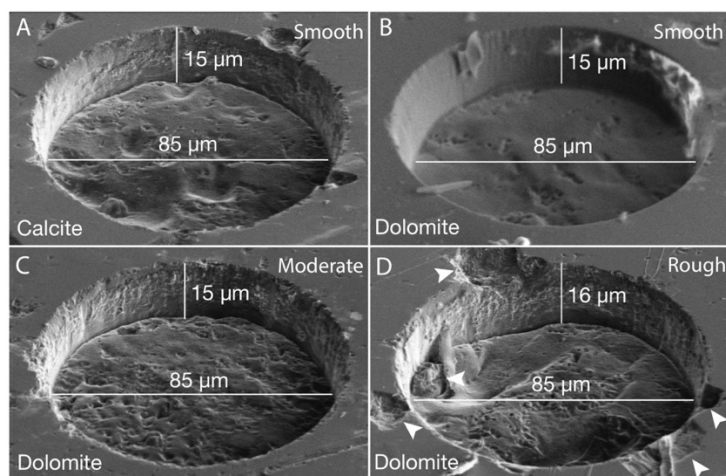
Figure 4: Ablation craters of calcite (A) vs. dolomite (B–D). Craters are compared to WC-1 and divided according to their geometry and crater bottom roughness into smooth (B), moderate (C) and rough (D). Uneven mass removal from crater rims are marked by white arrows on D.

In order to further study petrographic features of dolomites that may cause differences in ablation rate relative to the calcic

215 standard WC-1, and hens, differences in the resulted ages, we used several characterization techniques on our studied samples after LA analyses. Panchromatic back-scattered electron (BSE) images of representative samples show the distribution of grain size, tiling pattern and type of mineral zoning of dolomite rhombs, compared to 85 μm diameter LA crater (Fig. 5). Except for sample Tm-DV-1, where dolomite grains reach 200 μm, grain size and crystal zoning in all samples are usually smaller than spot size of 85 μm, making analyses of a single crystal impossible. Intracrystalline porosity may include other phases beside

220 dolomite, such as k-feldspar, pyrite, oxides and bituminous minerals (Fig. 5A; Olanipekun and Azmy, 2017) and is an important feature to be considered. When selecting locations for analyses pores should be avoided as much as possible.

In sample MU-1 the longest diagonal of dolomite crystals is ~60 μm. Dolomite cores of MU-1 appear much brighter in BSE compared to their concentric enclosing rims, probably due to higher Mg/Ca ratio and minor concentration of Fe (Fig. 5A; Olanipekun and Azmy, 2017). Dolomite crystals from sample KM-1 display mainly a concentric zoning pattern with a very

225 thin lamina separating core from rim. Abundant disseminated calcite inclusions are found in the cores but have relatively homogeneous rim sections (Fig. 5B). Such signature is likely to be associated with the mechanism of epigenetic dolomitization governed by diagenetic replacement of pore fluids and re-precipitation of dolomite (Putnis & Putnis, 2007; Olanipekun & Azmy, 2017).Within the large fragments of breccia sample EFN-1, a mixture of different zoning patterns can be seen: dolomite crystals that lack distinctive core to rim zones and crystals with two zones of bright cores and dark rims (Fig. 5C). The matrix

230 between the large fragments in this sample contain <50 μm isolated fragments of broken dolomite crystals embedded in homogeneous cement with bright BSE response (Fig. 5D). The BSE images highlight complexities in the chemical zoning of dolomite at sub-millimeter scale, i.e. distinct core and rim, semi-homogenized grains, or mixture of different grains. It is therefore important to acknowledge that spot analysis of these textures may result in age-mixing or averaging of the different phases.
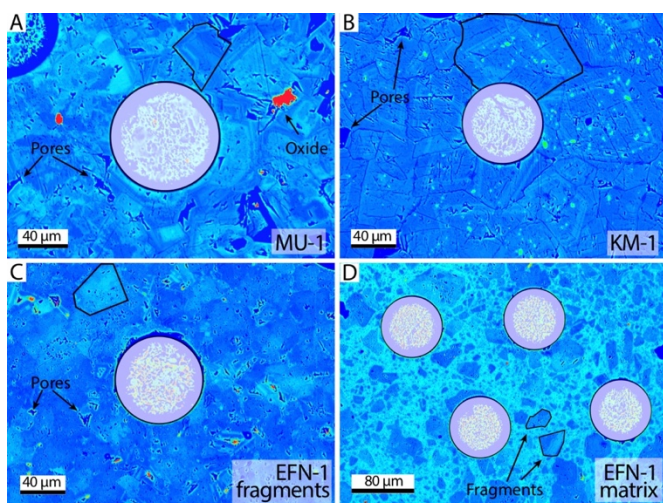
235

Figure 5: Panchromatic BSE images of samples MU-1 (A), KM-1 (B) and fragments and matrix of sample EFN-1 (C and D, respectively). BSE images are efficient in revealing the grain size of the sample, as well as porosity and additional intracrystalline phases. LA craters are marked by circles of 85 μm diameter. Representative grain boundaries are marked by black polygons.

3.3 Early phases and purity of dolomite

240   Another important aspect that needs to be considered in dolomite geochronology is the fact that dolomite recrystallization may preserve former remnants of calcite. X-ray diffraction (XRD) analyses on rock powders can help resolving this issue and were applied on the studied samples. Two samples were identified as pure dolomite (MU-1 and MU-2), three samples contain minor calcite component (MAM-3, MAM-7 and KM-1) and one sample encompass minor quartz component along with the dolomite (Tm-MU-2; Fig. 6A). As a complimentary, EBSD maps combined with EDS analyses can further distinguish between dolomite

245   and high-Mg calcite. For example, EBSD phase mapping identified ~45% dolomite, ~48% calcite and ~7% zero solution on sample KM-1. In samples MU-1 and MU-2 dolomite is much more abundant, with average of 67% dolomite, 25% calcite and 8% zero solution (Figure 6B and C). Although calcite phase is relatively abundant in these samples, EDS has identified more than 2:3 Mg/Ca ratio, indicating it is a high-Mg calcite. This support previous interpretations of replacement of calcite by dolomite. The difference between XRD and EBSD analyses imply that pseudosymmetry of high-Mg calcite and dolomite can

250   be unambiguously detected by *in-situ* EBSD phase mapping and not by XRD powder analyses. While the labor-intensive EBSD analysis is more sensitive in detecting calcite replacement than XRD, both methods are recommended for detecting impurities. In this study, less successful samples for dating (e.g. MAM-3 and MAM-7) are with higher calcite percentage relative to successfully dated samples (e.g. MU-1 and MU-2; Figure 6C–D).
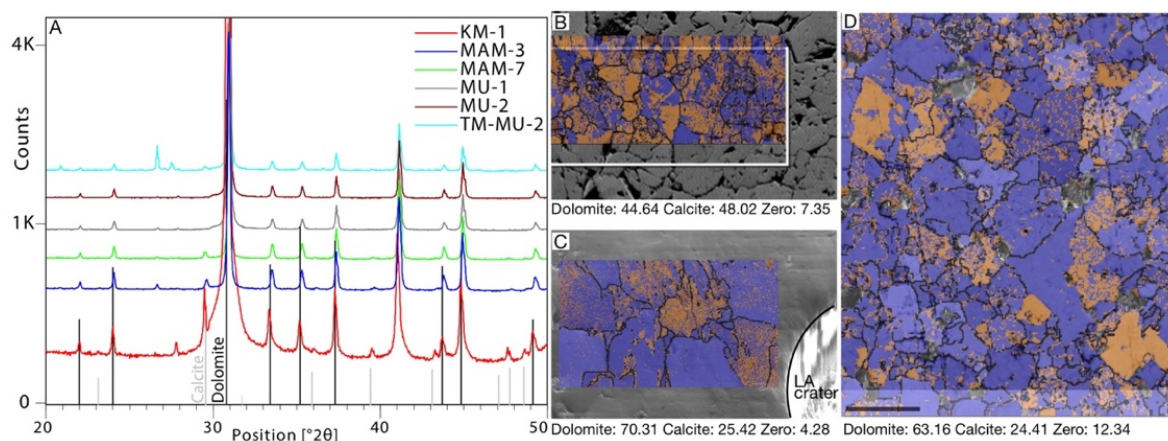
255   **Figure 6: (A) XRD results of the studied samples: all samples are composed entirely of dolomite (peaks above black vertical lines), while some samples show minor calcite contribution (grey vertical lines). Sample Tm-MU-2 shows additional minor peaks of quartz. EBSD phase maps of samples KM-1 (B), MU-1 (C) and MU-2 (D). Dolomite is marked in purple, calcite in orange and zero solutions and grain boundaries are marked in black.**

The WDS elemental maps of Fe, Mg and Ca were performed on sample KM-1 and are presented aside BSE image of the same
260   location. The zonings in dolomite grains seen in the BSE are visible in the Fe map (Fig. 7B). Under the resolution of the scan (<0.01 wt.%), Mg and Ca maps do not show chemical zoning, but Ca-rich and Mg-depleted zones can be seen within grain boundaries. These clusters are probably remnants of primary calcite that was later replaced by dolomite (Fig. 7C, D). The WDS mapping could be therefore used for detecting zoning and calcite impurities in dolomite samples and is highly recommended for samples with sparry grains.
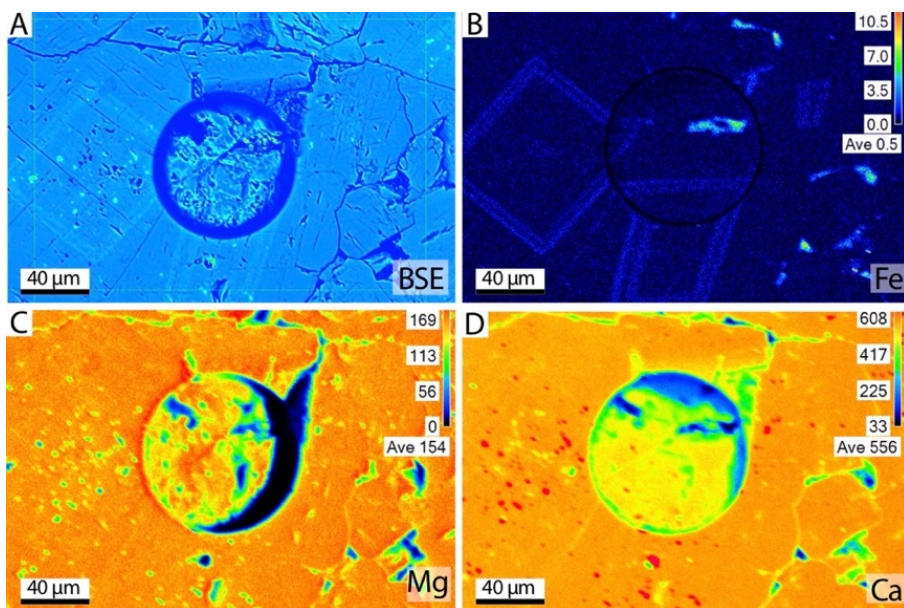
Figure 7: BSE image of LA crater on sample KM-1 (A) compared with WDS elemental maps of the same location (B-D). Zoning in dolomite rhomb is highlighted by Fe elemental map and absent on Mg and Ca. Mg-depleted and Ca-enriched clusters can be seen within the Fe rims of the dolomite crystals.

3.3 Average down-hole fractionation of RMs and selected unknowns

Results from samples MAM-1 and MAM-7 may be the most enigmatic of the sample set, as their ages are considerably older than expected, whereas other samples in this suite yield reasonably acceptable ages. One explanation might be that these samples had a different laser-induced elemental fraction (LIEF) than that of the rest of the sample suite and the calcite reference materials. Although similar in chemistry, these samples have a different texture from other samples, as they are micritic, rather than crystalline. Figure 8 shows stacked integration plots of the down-hole raw ^{207}Pb-corrected ^{206}Pb/^{238}U ratio of unknowns and RMs from each of two sessions in which a sample of either expected age (MU-2; session 1) or unexpected age (MAM-7; session 2) was analyzed. In both sessions, WC-1 (primary calcite RM), Duff Brown Tank (secondary calcite RM), NIST614 glass, and a zircon RM, Mud Tank (Black and Gulson, 1978), yielded consistent down-hole patterns, with zircon being the steepest, NIST614 with a minor negative slope and the calcite RMs in between. The down-hole pattern in MU-2 (run 1) was very similar to that of the primary calcite RM (WC-1) and it is therefore no surprise that it yielded the expected age. MAM-7 (run 2), however, yielded a negative down-hole fraction pattern, beyond that of any of the standards. Using NIST614 as a primary standard for calcite yields an age that is too old for calcite reference materials, and long-term correction factors typically range between 10–20% for ^{206}Pb/^{238}U. This is expected for the calcite vs. NIST glass fractionation patterns; the higher ^{206}Pb/^{238}U ratios of the calcite RMs down-hole would yield older ages relative to NIST. Interestingly, however, MAM-7 is older than expected, even though its ^{206}Pb/^{238}U ratio becomes smaller down-hole. This may indicate that the difference in ^{206}Pb/^{238}U ratios between measured and expected are caused by plasma-ionization differences between particles of MAM-7 and those of the reference materials and crystalline dolomite. A similar offset is seen in the zircon data; the steeper down-hole

fractionation of Mud Tank zircon would expect an age that is older than the reference value. Instead, the recovered age was typically ca. 20% younger than its accepted value. This further indicates the importance of analyzing samples of similar chemical and textural makeup when standardizing unknowns, and that drill rate is only one component of age offset.
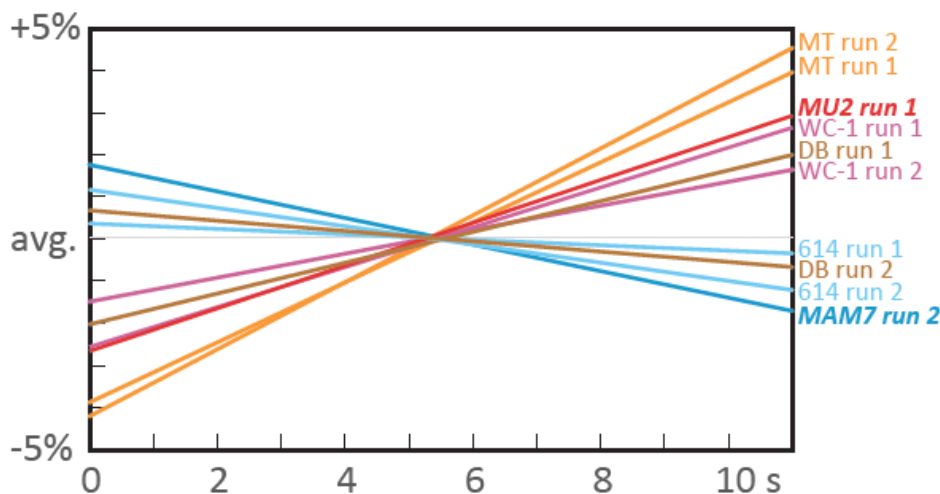
290

Figure 8. Average down-hole fractionation showing the difference between unknown samples and reference materials. The raw ^{207}Pb counts (corrected for baseline) are normalized to the average value and a linear fit shows the different fractionation trends between glass, zircon, calcite and dolomite in two different analytical runs.

3.5 Reevaluation of U–Pb results and interpretation

295 In sample EFN-1 fragments and matrix arrange along two different isochrons, forming a wedge with mixed ages between isochrons (Fig. 9). The ^{207}Pb/^{206}Pb interception occurs to the right of the concordia curve, resulting in higher common-Pb values for the older isochrone. The stratigraphic age of this faulted unit is considered Cenomanian and is known found in other regions as limestones, rather than dolomite. If dolomitization occurred after brecciation and cementation during a faulting event, a single age for both fragments and the matrix is expected. However, fragments and matrix yielded two distinct linear 300 trends, indicating that dolomitization of the host rock occurred before brecciation and dolomitization of the cement occurred during or after the faulting event at 6.5 ± 1 Ma (MSWD = 1.5; n = 32). Along the fragments two isochrones of acceptable ages can be identified, at 74 ± 3 and 58 ± 3. The different ages within the fragments may represent two separated diagenesis and dolomitization events of the rock before faulting, whereas cementation and dolomitization of the matrix occurred much later, at ~6 Ma.

305 A similar wedge pattern is also observed in sample MU-1, where the older isochrone corresponds to the expected stratigraphic age of this sample (Fig. 9). The result of sample MU-1 is ~30 Ma younger and may represent mixed ages. Out of 80 spot analyses, the older 13 dates form a reasonable isochron with age of 91 ± 6 Ma, with MSWD of 1.8. This age falls within the expected stratigraphic age and probably represents early diagenetic age for that sample. The youngest 38 spot analyses yield

an age of 53 ± 2 Ma, with MSWD of 2. The age of sample MU-2 (93 ±7), on the other hand, correspond to the expected

310 stratigraphic age for this unit. Despite its low-resolution isochrone, a similar pattern to MU-1 can be seen in sample KM-1, with an older age of 101 ± 11 Ma (MSWD =0.46; n = 15) and younger age of 56 ± 3 Ma (MSWD = 0.94; n=50). This repeating pattern can also be seen in the fragments of sample EFN-1 and may represent actual dolomitization event at ~55 Ma in these localities. Early Eocene dolomitization event is, however, not familiar in the local geological record and therefore may also reflect mixed ages of stratigraphic age (early diagenesis) and some younger event(s), similar to sample EFN-1, whereas a

315 young event correspond to the age of 6.5 Ma and association with faulting along the Dead Sea Fault.
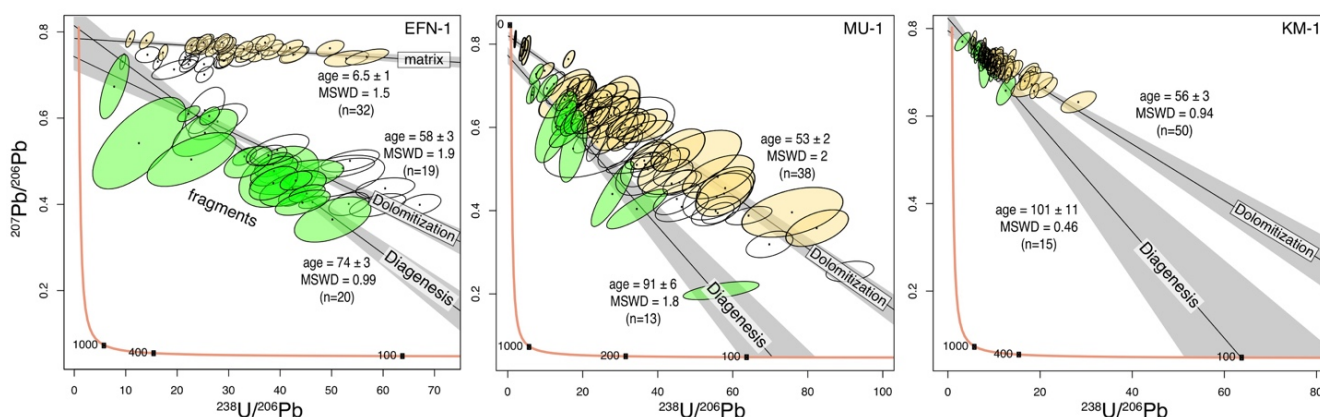
Figure 9: Age interpretation of U–Pb results for samples EFN-1, MU-1 and KM-1.

Acknowledgments

We thank Dr. Omri Dvir from the Hebrew University, Israel for the help with WDS maps and to Dr. Navot Morag from the

320 Geological Survey of Israel for the help with XRD analyses and interpretation. We thank Dr. Einat Nativ-Roth and Mrs. Roxana Golan from the Ilse Katz Institute for Nanoscale Sciences and Technology, Ben-Gurion University of the Negev for their help with SEM imaging and EBSD mapping. This study was supported by the Israeli Government (under the Geological Survey of Israel, Dead Sea, project 40709).

References

325 Ahm, A. S. C., Bjerrum, C. J., Blättler, C. L., Swart, P. K., & Higgins, J. A.: Quantifying early marine diagenesis in shallow-water carbonate sediments, *Geochimica et Cosmochimica Acta*, 236, 140-159, 2018.

Beyth, M., Longstaffe, F. J., Ayalon, A., & Matthews, A.: Epigenetic alteration of the Precambrian igneous complex at Mount Timna, southern Israel: Oxygen-isotope studies, *Israel Journal of Earth Sciences*, *46*, 1-11, 1997.

Beyth, M., & Heimann, A.: The youngest igneous event in the crystalline basement of the Arabian-Nubian Shield, Timna

330 Igneous Complex, *Isr. J. Earth Sci*, 48, 113-120, 1999.

Beyth, M., Segev, A., Bartov, Y.: Geological Map of Israel. Sheet 25-IV Be'er Ora, Scale 1:50,000, Israel Geological Survey, Jerusalem, 1999.

Frisia, S., Borsato, A., & Hellstrom, J.: High spatial resolution investigation of nucleation, growth and early diagenesis in speleothems as exemplar for sedimentary carbonates, *Earth-Science Reviews*, 178, 68-91, 2018.

335 Godeau, N., Deschamps, P., Guihou, A., Leonide, P., Tendil, A., Gerdes, A., Hamelin, B. and Girard, J.P.: U-Pb dating of calcite cement and diagenetic history in microporous carbonate reservoirs: Case of the Urgonian Limestone, France, *Geology*, 46, 247-250, 2018.

Guillong, M., Wotzlaw, J.-F., Looser, N., and Laurent, O.: New analytical and data evaluation protocols to improve the reliability of U–Pb LA-ICP-MS carbonate dating, *Geochronology Discuss*, in review, 2020.

340 Gregg, J. M., & Sibley, D. F.: Epigenetic dolomitization and the origin of xenotopic dolomite texture, *Journal of Sedimentary Research*, 54, 908-931, 1984.

Hill, C. A., Polyak, V. J., Asmerom, Y., & P. Provencio, P.: Constraints on a Late Cretaceous uplift, denudation, and incision of the Grand Canyon region, southwestern Colorado Plateau, USA, from U-Pb dating of lacustrine limestone, *Tectonics*, *35*, 896-906, 2016.

345 Hodson, K.R., Crider, J.G. and Huntington, K.W.: Temperature and composition of carbonate cements record early structural control on cementation in a nascent deformation band fault zone: Moab Fault, Utah, USA, *Tectonophysics*, *690*, 240-252, 2016.

Kohn, B, Weissbrod, T, Chung, L, Farley, K, Bodorkos, S.: Low-temperature thermochronology of francolite: Insights into timing of Dead Sea Transform motion, *Terra Nova*, 31: 205– 219, 2019.

350 Li, Q., Parrish, R. R., Horstwood, M. S. A., & McArthur, J. M.: U–Pb dating of cements in Mesozoic ammonites, *Chemical Geology*, 376, 76-83, 2014.

Ludwig, K. R.: Isoplot/Ex, v. 3.75, *Berkeley Geochronology Center Special Publication*, *5*, 75, 2012.

Machel, H. G.: Concepts and models of dolomitization: a critical reappraisal, *Geological Society, London, Special Publications*, 235, 7-63, 2004.

355 Nuriel, P., Weinberger, R., Kylander-Clark, A.R.C., Hacker, B.R. and Craddock, J.P.: The onset of the Dead Sea transform based on calcite age-strain analyses, *Geology*, 45, 587-590, 2017.

Nuriel, P., Wotzlaw, J., Ovtcharova, M., Vaks, A., Stremtan, C., Šala, M., Roberts, N., and Kylander-Clark, A.R.C.: The use of ASH-15 flowstone as matrix-matched standard for laser-ablation geochronology of calcite, *Geochronology discuss*, *in-review*, 2020.

360 Olanipekun, B. J., & Azmy, K.: *In situ* characterization of dolomite crystals: Evaluation of dolomitization process and its effect on zoning, *Sedimentology*, *64*, 1708-1730, 2017.

Parnes, A.: Late Lower Cambrian trilobites from the Timna area and Har Amram (southern Negev, Israel), *Israel Journal of Earth Sciences*, *20*, 179-205, 1971.

365 Parrish, R.R., Parrish, C.M. and Lasalle, S.: Vein calcite dating reveals Pyrenean orogen as cause of Paleogene deformation in southern England, *Journal of the Geological Society*, 175, 425-442, 2018.

Paton, C., Woodhead, J. D., Hellstrom, J. C., Hergt, J. M., Greig, A., and Maas, R.: Improved laser ablation U-Pb zircon geochronology through robust downhole fractionation correction, *Geochemistry Geophysics Geosystems*, 11, 2010.

Putnis, A. and Putnis, C. V.: The mechanism of re- equilibration of solids in the presence of a fluid phase, *Journal of Solid-*
370 *State Chem.*, 180, 1783–1786, 2007.

Ring, U. and Gerdes, A.: Kinematics of the Alpenrhein-Bodensee graben system in the Central Alps: Oligocene/Miocene transtension due to formation of the Western Alps arc, *Tectonics*, 35, 1367-1391, 2016.

Roberts, N.M.W. and Walker, R.J.: U-Pb geochronology of calcite-mineralized faults: Absolute timing of rift-related fault events on the northeast Atlantic
375 margin, *Geology*, 44, 531-534, 2016.

Roberts, N. M. W., Rasbury, E. T., Parrish, R. R., Smith, C. J., Horstwood, M. S. A., and Condon, D. J.: A calcite reference material for LA- ICP-MS U-Pb geochronology, *Geochemistry Geophysics Geosystems*, 18, 2807-2814, 2017.

Roberts, N.M., Drost, K., Horstwood, M.S., Condon, D.J., Chew, D., Drake, H., Milodowski, A.E., McLean, N.M., Smye, A.J., Walker, R.J. and Haslam, R.: Laser ablation inductively coupled plasma mass spectrometry (LA-ICP-MS) U-Pb
380 carbonate geochronology: strategies, progress, and limitations, *Geochronology discuss*, 2, 33-61, 2020.

Sass, E.: Microphotometric determination of preferred orientation in undeformed dolomites, *Science*, 165, 802-803, 1969.

Sass, E., and Bein, A.: Platform carbonates and reefs in the Judean Hills, Carmel and Galilee, *in* Proceedings Tenth International Congress on Sedimentology. International Association of sedimentologists, Jerusalem, Field guidebook, 239-274, 1978.

385 Sass, E., Dekel, A., Sneh, A.: Geological Map of Israel. Sheet 5-II Umm El Fahm, Scale 1:50,000. Israel Geological Survey, Jerusalem, 2013.

Segev, A., Sass, E., Ron, H., Lang, B., Kolodny, Y., and McWilliams, M.: Stratigraphic, geochronologic, and paleomagnetic constraints on Late Cretaceous volcanism in northern Israel, *Israel Journal of Earth Sciences*, 51, 2002.

Segev, A., Sass, E.: Geological Map of Israel. Sheet 3- III Atlit, Scale 1:50,000. Israel Geological Survey, Jerusalem, 2009.

390 Segev, A.: ^{40}Ar/^{39}Ar and K–Ar geochronology of Berriasian–Hauterivian and Cenomanian tectonomagmatic events in northern Israel: implications for regional stratigraphy, *Cretaceous Research*, *30*, 810-828, 2009.

Segev, A.: Major unconformities in the stratigraphic succession in the Timna-Eilat region and their relation to copper and manganese mineralization cycles, *Isr. Geol. Soc. Field Trips Guide. Elat*, 154-188, 2016.

Sneh, A., Avni Y.: Geological Map of Israel. Sheet 11- II Jerusalem, Scale 1:50,000. Israel Geological Survey, Jerusalem,
395 2016.

Stacey, J.T. and Kramers, J.: Approximation of terrestrial lead isotope evolution by a two-stage model. *Earth and planetary science letters*, 26, 207-221, 1975.

Tera, F., and Wasserburg, G. J.: U-Th-Pb systematics in three Apollo 14 basalts and the problem of initial Pb in lunar rocks, *Earth and Planetary Science Letters*, *14*, 281-304, 1972.

400   Vermeesch, P.: IsoplotR: A free and open toolbox for geochronology, *Geoscience Frontiers*, *9*, 1479-1493, 2018.

Warren, J.: Dolomite: occurrence, evolution and economically important associations, *Earth-Science Reviews*, 52, 1-81, 2000.